Thermoelectric properties of non-stoichiometric $CaMnO_{3-\delta}$ composites formed by redox-activated exsolution

Sathya Prakash Singh[1], Nikola Kanas[1], Temesgen D. Desissa[2,*], Mari-Ann Einarsrud[1], Truls Norby[2], and Kjell Wiik[1]

[1]Department of Materials Science and Engineering, NTNU Norwegian University of Science and Technology, NO-7491Trondheim, Norway

[2]Department of Chemistry, Centre for Materials Science and Nanotechnology, University of Oslo, FERMiO, Gaustadalléen 21, NO-0349 Oslo, Norway

Keywords: thermoelectrics, oxides, composites, exsolution, figure-of-merit

Abstract

A novel synthesis route for preparing well-defined composites based on CMO has been established taking advantage of the unique phase relations in the system Ca-Mn-O at reducing- and oxidizing atmosphere, respectively. Samples corresponding to stoichiometric CMO and composites with 5 and 10 vol % of Ruddlesden-Popper ($Ca_4Mn_3O_{10}$)- and spinel ($CaMn_2O_4$)-phases, respectively, were prepared with final densities >91 %. The presence of secondary phases significantly enhanced the electrical conductivity compared to stoichiometric CMO. The highest electrical conductivity was observed for CMO with 10 vol % spinel varying between 55 and 75 S/cm at temperatures between 100 and 900 °C. This composition also exhibited the highest figure-of-merit (zT) in this study, reaching 0.083 at 800 °C.

1. Introduction

Numerous industrial processes (boilers, combustion engines, furnaces) produce ample amounts of waste heat and recovering this heat to useful energy is one viable route to reduce greenhouse gas emissions and at the same time improve the economy of the processes where recovery is conceivable [1]. Thermoelectric generators (TEGs) offer a simple and robust

* Present address: Department of Materials Science and Engineering, Adama Science and Technology University, P.O.Box: 1888, Adama, Ethiopia.

technology for converting heat directly into electricity. The efficiency of a given material is dictated by its figure-of-merit, *zT*,

$$zT = \frac{S^2 \sigma T}{\kappa} \qquad (1)$$

where S is the Seebeck coefficient, κ is the total thermal conductivity and σ is the electrical conductivity [2]. The power factor is defined as $P = S^2\sigma$, and for applications of TEGs where the maximum electrical power generation is of importance (infinite heat source) the materials selection should be focused on high power factors, and the reduction in thermal conductivity becomes less important [3-5]. For applications where maximum conversion efficiency is the key factor (limited heat source) the optimization of *zT* is important [4].

Currently, the most efficient thermoelectric materials are heavy metal alloys which are restricted to medium temperatures due to oxidation or melting, high cost and toxicity [6]. To harvest waste heat at higher temperatures (*e.g.* 800-900 °C) in ambient atmosphere, oxides represent a favorable choice due to their stability. Whereas p-type oxides such as $Ca_3Co_{3.92}O_{9-\delta}$ (CCO) exhibit good thermoelectric properties [7], the choices of n-type oxides are fewer. Although Al-doped ZnO has been reported with rather high *zT* at elevated temperatures, there are challenges associated with long-term stability as reduction in performance is observed over time [8-9].

Here we have chosen n-type oxide, $CaMnO_{3-\delta}$ (CMO) as a backbone structure for our study. CMO is usually reported as a line-compound consistent with a 1:1 ratio between the fully occupied A- and B-sites in the perovskite [10]. The stable polymorph in air at ambient temperature is orthorhombic, transforming into a tetragonal phase at 896 °C and cubic phase above 913 °C [11]. Heating CMO will increase the fraction of 3-valent Mn corresponding to increased δ in $CaMnO_{3-\delta}$, affecting both the electronic conductivity, and the Seebeck coefficient. The variation in σ and S with pO_2 and T for CMO is reported by Schrade *et al.* [12], whereas the phase transitions in terms of pO_2 and T is documented in [13-15].

Most of the research on thermoelectric properties of CMO is on doped and co-doped compositions. Zhu *et al.* [16] co-doped CMO with Dy and Ho and measured *zT*=0.23 at 700 °C whereas Su *et al.* [17] co-doped with Dy and Yb and reported *zT*=0.27 at 800 °C. Thiel *et al.* [20] reached 0.25 at 950 °C for tungsten doped CMO. However, the highest *zT* to date is reported by Bocher *et al.* [18] for Nb-doped CMO ($CaMn_{0.98}Nb_{0.02}O_{3-\delta}$) reaching 0.32 at 800 °C. Only a few

studies [19-22] have reported *zT*-values for undoped $CaMnO_{3-\delta}$ from room temperature to high temperatures in air. The highest *zT* was reported by Thiel *et al.* [20] measuring 0.15 at 900 °C in air, whereas both Zhu *et al.* [19] and Flahaut *et al.* [22] reported only 0.06 and 0.05, respectively, at similar temperatures. There are several strategies to increase *zT*, such as minimizing the thermal conductivity by enhanced phonon scattering due to increased density of grain boundaries (nanosized grains) [23] as well as presence of secondary phases. Doping with heavy elements is also a viable route to reduce thermal conductivity. The electronic conductivity of oxides is generally low, and enhancement is usually approached by appropriate donor doping in the case of *n-type* oxides.

In this contribution, our main objective is to present a new concept for the preparation of oxide composites as TE materials by taking advantage of a redox-activated exsolution. Pure CMO is chosen as the material of interest as in reducing conditions complete solid solubility exists in the whole composition range CaO-MnO (rock salt structure) [24-25], whereas under oxidizing conditions there are a number of Ruddlesden-Popper (RP, $Ca_4Mn_3O_{10}$) phases at the Ca-rich side and a spinel (Sp, $CaMn_2O_4$) phase (marokite) at the Mn-rich side [10]. This gives an unique opportunity to control the type, amount and size of exsoluted secondary phases [26]. We synthesized single-phase materials under reducing conditions with variable ratios between Ca and Mn, and exsolved the secondary phases by annealing at oxidizing conditions at elevated temperatures. Here we report the variation in TE-properties between room temperature and 800-900 °C in synthetic air for nominal stoichiometries of $Ca_xMnO_{3-\delta}$ (x= 1.028, 1.014, 1.000, 0.966 and 0.934). According to the phase diagram [10] these stoichiometries correspond to 10 and 5 vol% of a RP phase at the Ca-rich side and 5 and 10 vol% of a Sp phase at the Ca-deficient side. To the best of our knowledge this is the first systematic study of the variation in TE-properties for CMO with the presence of secondary phases generated by redox-activated exsolution and this method can also further be developed for doped-CMO materials.

2. Materials and Methods

2.1. Material synthesis by a novel route

Polycrystalline, stoichiometric $CaMnO_{3-\delta}$ and $CaMnO_{3-\delta}$ composites were synthesized by a novel two-step synthesis route as shown in Fig. 1. In the first step, calcium carbonate ($CaCO_3$, 99.99 %, Merck) and manganese oxide (MnO_2, 99.9 %, Sigma Aldrich) were mixed according to the nominal stoichiometries and planetary milled (PM 100, Retsch) with yttria-stabilized zirconia (YSZ) balls in ethanol for 2 h and subsequently dried in a rotavapor (Butch Rotavapor). The dry powder was heated for 6 h at 1245 °C in 5 % H_2/Ar-atmosphere to form a single-phase material.
In the second step, the obtained product was crushed in an agate mortar and planetary milled for 30 min, prior to uniaxial pressing followed by cold isostatic pressing (CIP) at 200 MPa into the appropriate sample shape, (bar-shaped for electrical conductivity and Seebeck measurements (20 mm x 5 mm x 3 mm), and disc shaped for thermal conductivity measurements (15 mm^{ø} and thickness 3 mm). The green bodies were heated to 850 °C in 5 % H_2/Ar-atmosphere followed by a change to N_2-atmosphere and further heating to 1350 °C where sintering took place for 4 h. Finally, the atmosphere was switched to synthetic air for the remaining 25-40 h to exsolve the secondary phases (Fig. 1, Step 2).
The two-step method was carried out in a tubular furnace, and the rate of gas flow was 80 mL/min. The heating rate was 200 °C/h whereas the rate of cooling was 60 °C/h. Synthesis of the pure secondary phases (Sp and RP) was done in a similar way following Step 1-2 described in Fig. 1. Nomenclature and experimental parameters are given in Tab. 1.

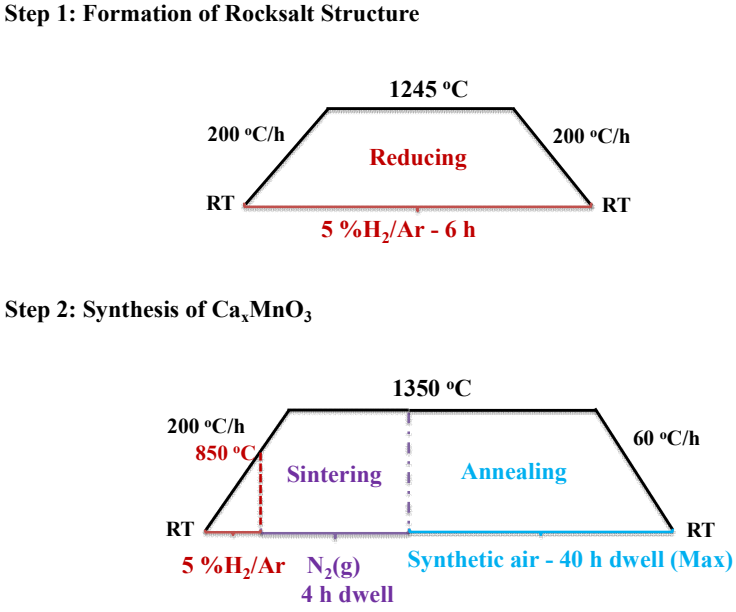

Figure 1. Step 1: Formation of rock salt structures in 5 % H_2 /Ar at 1245 °C. Step 2: Synthesis of nominal stoichiometries Ca_xMnO_3 where x = 1.028, 1.014, 1.00, 0.966 and 0.934. The pure RP ($Ca_4Mn_3O_{10}$) and Sp ($CaMn_2O_4$) phases were synthesized in the same way.

2.2. Materials characterization

The samples were analyzed by X-ray diffraction (XRD) of finely ground powder (Bruker AXS D8-Advance X-ray diffractometer) using Cu Kα radiation and a Lynxeye XE detector, with counting time 0.2 sec in the range 10-75º (2θ angles) and 0.92 º/minute scan rate. XRD analysis was performed both prior to and after Step 2.

Table 1. Nomenclature, nominal composition and annealing time in synthetic air for all samples. The following nomenclature is applied: CMO ($CaMnO_{3-\delta}$), RP (Ruddlesden-Popper, $Ca_4Mn_3O_{10}$), Sp (Spinel/Marokite, $CaMn_2O_4$). The theoretical densities of the composites are calculated based on data from [27-30] using the law of mixtures.

x in Ca_xMnO_3	Nomenclature	Nominal composition	Theoretical density, ($g \cdot cm^{-3}$)	Annealing time (h/ condition)
NA	Rock salt	Rock salt ($CaMnO_2$)	4.25 [26]	4/N_2
1.028	CMO(10RP)	10 vol% RP, 90 vol % $CaMnO_3$	4.55	40/air
1.014	CMO(5RP)	5 vol% RP, 95 vol % $CaMnO_3$	4.56	40/air
1.0	CMO	Single phase $CaMnO_{3-\delta}$	4.57 [25]	40/air
0.966	CMO(5Sp)	5 vol% Sp, 95 vol% $CaMnO_3$	4.58	25/air
0.934	CMO(10Sp)	10 vol% Sp, 90 vol% $CaMnO_3$	4.58	25/air
NA	Sp	$CaMn_2O_4$, Marokite	4.68 [28]	25/air
NA	RP	$Ca_4Mn_3O_{10}$	4.34 [27]	40/air

Microstructures were assessed by scanning electron microscopy (SEM, Hitachi S3400N), on both fracture surfaces and polished/thermally etched surfaces (10 h in air at 1100 °C) to visualize grain

size. Densities/porosities were determined by the Archimedes method using isopropanol as immersion liquid. Direct current (DC) conductivity measurements were performed by using a DC standard 4-point technique (in-house built setup [31]) at temperatures between RT and 900 °C in synthetic air at 100 °C temperature intervals and thermal equilibration at each temperature. Seebeck coefficient measurements were done in synthetic air at temperatures between RT and 900 °C using Omega software and a ProboStat™ sample holder (NORECS, Norway) inserted into a vertical tube furnace, utilizing the inherent temperature gradient along the furnace length. Thermal conductivity was measured by the laser flash method (Netzsch 457 Microflash®) at temperatures between RT and 800 °C.

3. Results and Discussion

3.1. Phase relations

XRD patterns of all materials heat treated according to Fig. 1 are presented in Fig. 2. The insets in Fig. 2 show clearly the presence of the exsolved secondary phases (RP and Sp) in CMO(5RP), CMO(10RP), CMO(5Sp) and CMO(10Sp). The intensity of the diffraction lines from RP and Sp is increasing with increasing volume fraction of the secondary phase (nominal 5 and 10 vol%). The XRD patterns of the separately synthesized secondary phases given in Fig. 3 corresponds to phase pure Sp-phase whereas there are some traces of $CaMnO_3$ in the RP phase.

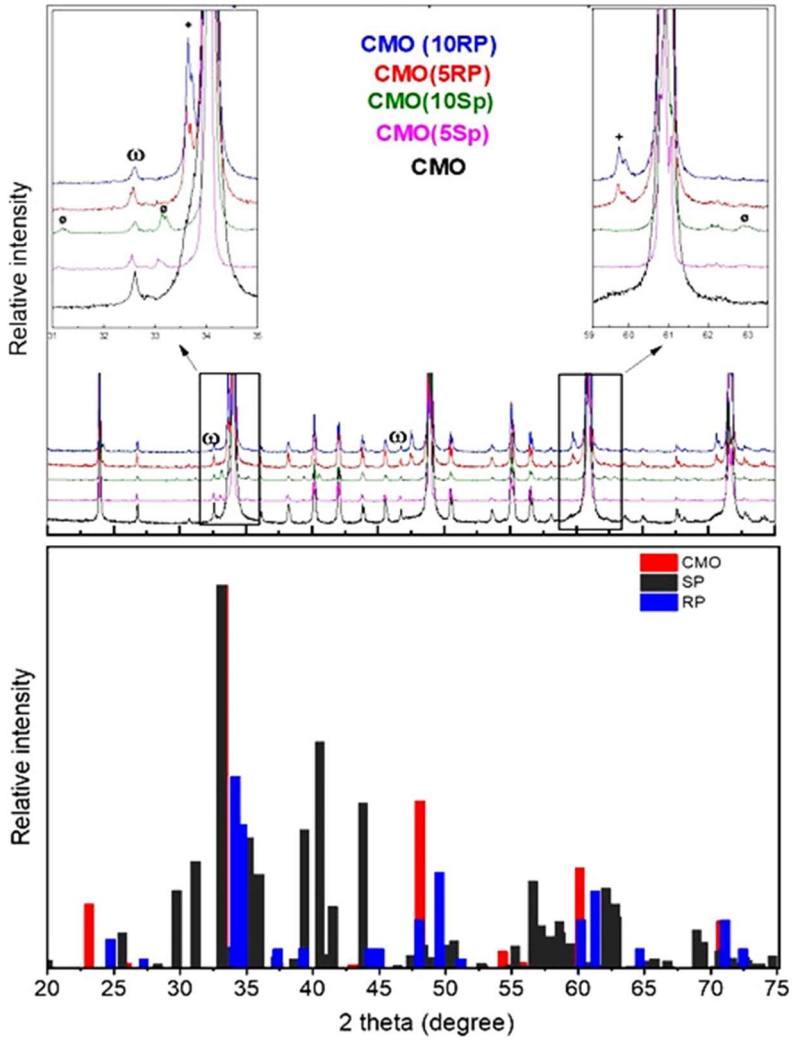

Figure 2. Top: XRD patterns of CMO (black), CMO(10Sp) (green), CMO(5Sp) (pink), CMO(10RP) (blue) and CMO(5RP) (red). Legend: Ø (Sp, PDF 04-015-3975), + (RP, PDF 00-018-0298). The minor diffraction lines marked with ω are artifacts due to secondary radiation from tungsten ($WL_{\alpha 1}$) originating from the X-ray tube. The remaining peaks are due to the presence of orthorhombic CMO (pnma-62, PDF 04-014-8192). Bottom: Separate XRD-pattern for CMO, Sp and RP, according to PDF-data.

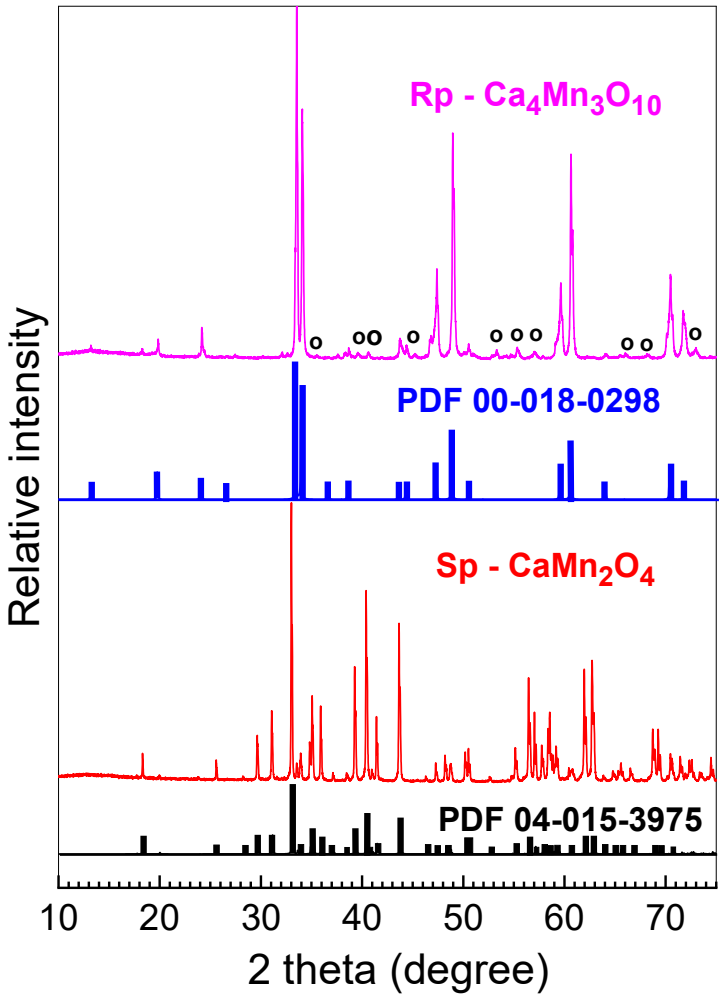

Figure 3. XRD patterns of Ruddlesden Popper phase $Ca_4Mn_3O_{10}$, (Blue: PDF 00-018-0298) and marokite phase $CaMn_2O_4$ (Black: PDF 04-015-3975). Secondary CMO phase in the RP phase is marked with o.

3.2. Density, microstructure and composition

The density and porosity reported in Tab. 2 confirm a high density for all samples except the RP phase which reaches only 85 %.

Table 2. Density (± 2 %) and porosity for all samples.

Sample	Bulk density (%)	Porosity (%)	
		Open	Closed
Rock salt	90	2	8
CMO(10RP)	92	1	7
CMO(5RP)	92	2	6
CMO	91	2	7
CMO(5Sp)	94	1	5
CMO(10Sp)	95	0	5
Sp	97	0	3
RP	85	13	2

The SEM-images for the rock salt precursor phase, prior to annealing in synthetic air, as well as pure CMO and CMO-composites with 10 vol% RP and Sp are presented in Fig. 4. There is a reasonable agreement between porosities given in Tab. 2 and micrographs given in Fig. 4. The grain size of the major phase (CMO) for all annealed samples is between 5 and 25 μm. The back scatter electron (BSE) image, as shown in Fig. 4c for CMO(10RP)indicates that the RP-phase nucleates and grows in a random way with a plate/needle-like morphology. The BSE-image of CMO(10Sp) (Fig. 4d) shows that the exsolution of the spinel phase (bright areas) takes place both at triple points and at grain boundaries. XRD and SEM analysis (Figs. 2 and 4) confirm the applicability of redox-activated exsolution as a method to produce well defined composites in the Ca-Mn-O system.

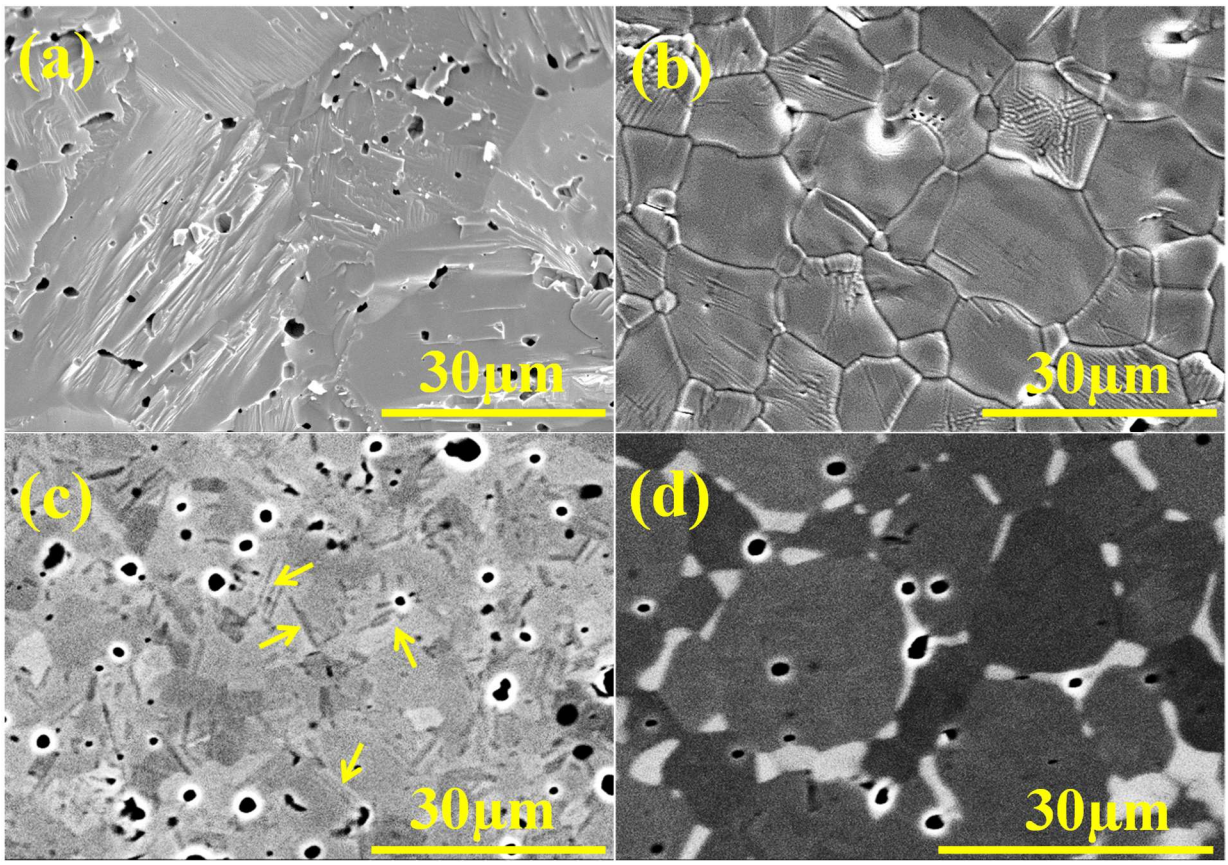

Figure 4. SEM images of a) fracture surface of a sample sintered in reducing atmosphere (rock salt structure), b) polished and thermally etched stoichiometric $CaMnO_3$ (CMO), c) polished 10 vol% RP (CMO(10RP)), and d) polished 10 vol% Sp (CMO(10Sp)). a) and b) are secondary electron (SE) images while c) and d) are back scattered electron (BSE) images. Arrows in c) show the presence of the RP-phase.

3.3. Thermoelectric properties

3.3.1. Electrical conductivity

The electrical conductivities for all samples are shown in Fig. 5. At temperatures below 500 °C, the kinetics of the oxygen exchange reaction was slow and we assume that the defect chemistry is "frozen", corresponding to a fixed and temperature independent concentration of oxygen vacancies. At temperatures above 500 °C, equilibration with synthetic air was possible within a reasonable time, corresponding to an increasing concentration of oxygen vacancies with temperature. A significant increase in electrical conductivity at high temperatures is consistent

with polaron hopping being the dominant mechanism. The electrical conductivity will thus be defined by the ratio between Mn^{3+} and Mn^{4+} at the B-site of the perovskite, as thoroughly explained in the literature [12, 19-22].

At lower temperatures there is a huge diversity in σ with temperature and CMO shows a low conductivity (4-7 $S \cdot cm^{-1}$), in line with existing literature [19-22]. However, a significant enhancement in σ is observed for all samples containing secondary phases. Comparing conductivity between CMO and the CMO-composites at 100 °C, σ is enhanced by a factor of approximately 3 for CMO(5RP) and CMO(10RP), a factor > 5 for CMO(5Sp) and more than one order of magnitude for CMO(10Rp). Based on the low conductivities of the secondary phases these results are intuitively surprising. As shown in Fig. 5b, the conductivity of the spinel phase varies between < $2 \cdot 10^{-3}$ and 0.3 $S \cdot cm^{-1}$ at temperatures between 200 and 900 °C while for the RP phase variations between 1 and 15 $S \cdot cm^{-1}$ in the same temperature interval are observed. This rule out an enhanced conductivity due to the possible existence of a percolating and continuous secondary phase with a high electrical conductivity. The highest conductivity is observed for the CMO(10Sp) sample, which is a composite with 10 vol% Sp and 90 vol% CMO, that is, a combination of a rather moderate electronic conductor and an almost electrical insulating phase. The observed behavior is suggested to be due to phenomena at the interface between CMO and Sp. Pryds and Esposito have published a comprehensive review on how electrical properties of composite oxides may be affected by phenomena taking place at the interfaces between oxide phases [32]. They show that combining phases with inherently low conductivities or even electrical insulating phases resulted in composites with significantly enhanced total conductivity, either due to enhanced mobility and/or concentration of charge carriers. The reason for this behavior is not unambiguously established, but may be related to strain, space charge at interface or the "polar catastrophe model" [33]. CMO(10Sp) clearly has a large number of interfaces between CMO and the Sp phase (Fig. 4 d), and the observed increase in conductivity may be due to enhanced mobility and/or enhanced concentration of charge carriers at the interface. The observed increase in conductivity observed for the composites with RP-phases may be explained along the same lines, although a more modest increase in σ is observed for these composites. These results are considered encouraging with respect to a further enhancement of the thermoelectric properties of undoped CMO and may also apply for donor doped CMO.

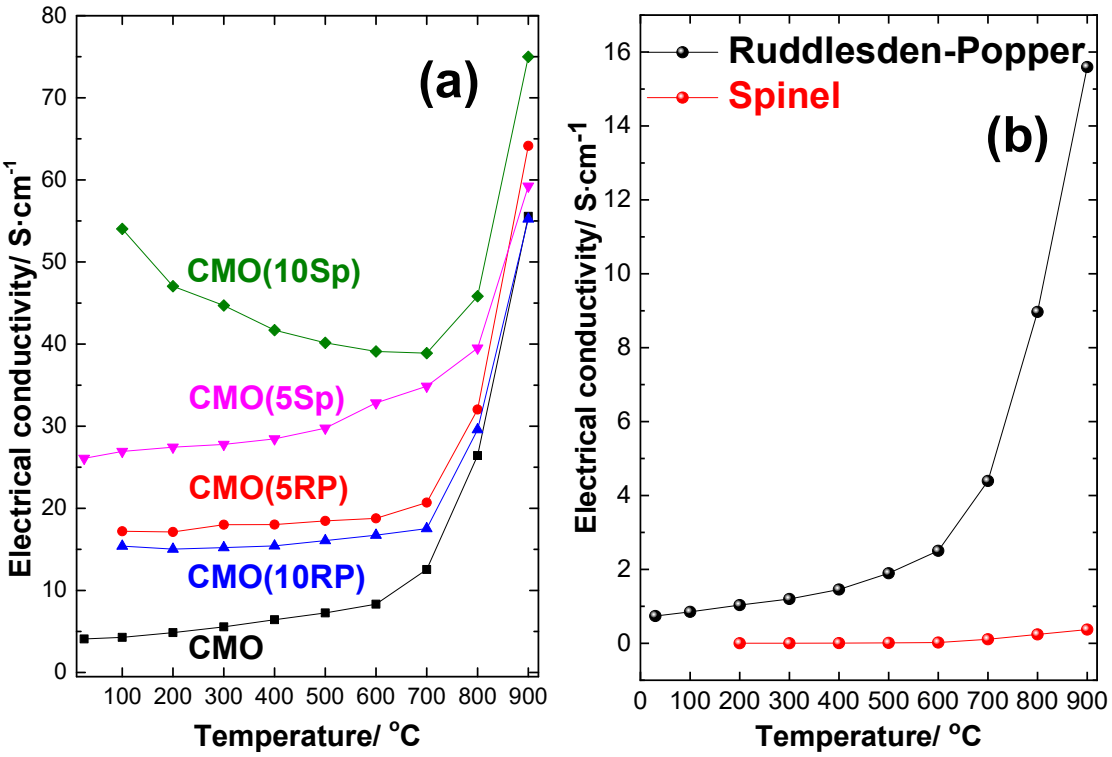

Figure 5. Variation in electrical conductivity (± 1 %) with temperature in air for a) CMO and CMO- composites measured in synthetic air, b) Ruddlesden-Popper (black) and Spinel (red).

3.3.2. Seebeck coefficient and Jonker plot

The Seebeck coefficients are given in Fig. 6 and show negative values consistent with *n-type* electronic conductivity. At moderate temperatures, CMO shows the highest $|S|$ while the lowest value is given by CMO(10Sp). Whereas $|S|$ for CMO steadily decreases with temperature, all composites show a relatively temperature independent plateau at intermediate temperatures, prior to a significant decrease at even higher temperatures. For metals or degenerate semiconductors, the relationship between *S* and carrier concentration, *n*, is given by Eq. 2 [6],

$$S = \frac{8\pi^2 k_B^2}{3eh^2} m^* T \left(\frac{\pi}{3n}\right)^{\frac{2}{3}} \qquad (2)$$

where k_B is the Boltzmann constant, e is the elementary charge, h is Plank's constant, m^* is the effective mass of charge carrier, and T is the absolute temperature. According to Eq. 2, $|S|$ will be inversely proportional to the carrier concentration, $n^{2/3}$. Comparing the conductivity data in Fig. 5 with Seebeck coefficients in Fig. 6 the general feature is a decreasing S with increasing σ at T<600 °C. At even higher temperatures there is a significant increase in conductivity for all materials due to the polaron hopping conductivity mechanism and the corresponding S values for the materials are seen to converge to a common value around -150 μVK^{-1} at 900 °C.

The variation in Seebeck coefficients for RP and Sp phases are given in Fig. 6b. In line with the low electronic conductivities reported in Fig. 5 b, large $|S|$-values are observed at moderate temperatures and seemingly converging at high temperatures consistent with the increasing electronic conductivity. It should be noted that the RP phase exhibits a rather large increase in conductivity as opposed to the Sp phase (Fig. 5b), even so the Seebeck coefficients for both phases are comparable at the highest temperature.

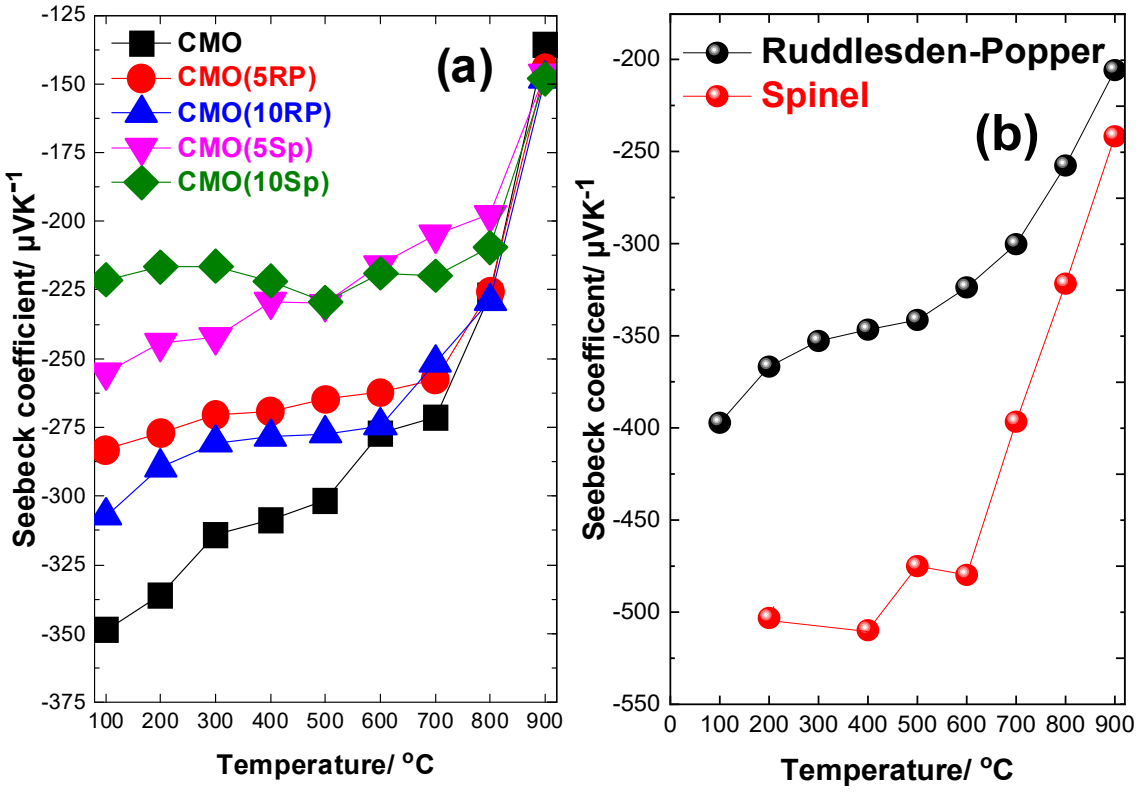

Figure 6. Variation in Seebeck coefficient with temperature in air for (a) CMO and CMO composites and (b) Ruddlesden-Popper (black) and spinel (red) phases. The uncertainty in S is within ± 5 %.

A Jonker plot shows the relation between the Seebeck coefficient and the electrical conductivity and is based on the following equation [34]

$$S = \frac{k_B}{e}\left[\ln\sigma - \ln e\mu N_c \exp(A)\right] \quad (3)$$

where μ is the carrier mobility, N_c is the density of states (DOS) and A is a transport constant ($0 \le A \le 2$). If the mobility, DOS and the conduction mechanism are unaffected by the carrier concentration, a plot of S vs. $ln\sigma$ should give a straight line with slope $k_B/e = \pm 86.15$ μV/K and an intercept given by the product between DOS and the mobility [35]. A Jonker plot is provided in Fig. 7 for CMO and the CMO-composites.

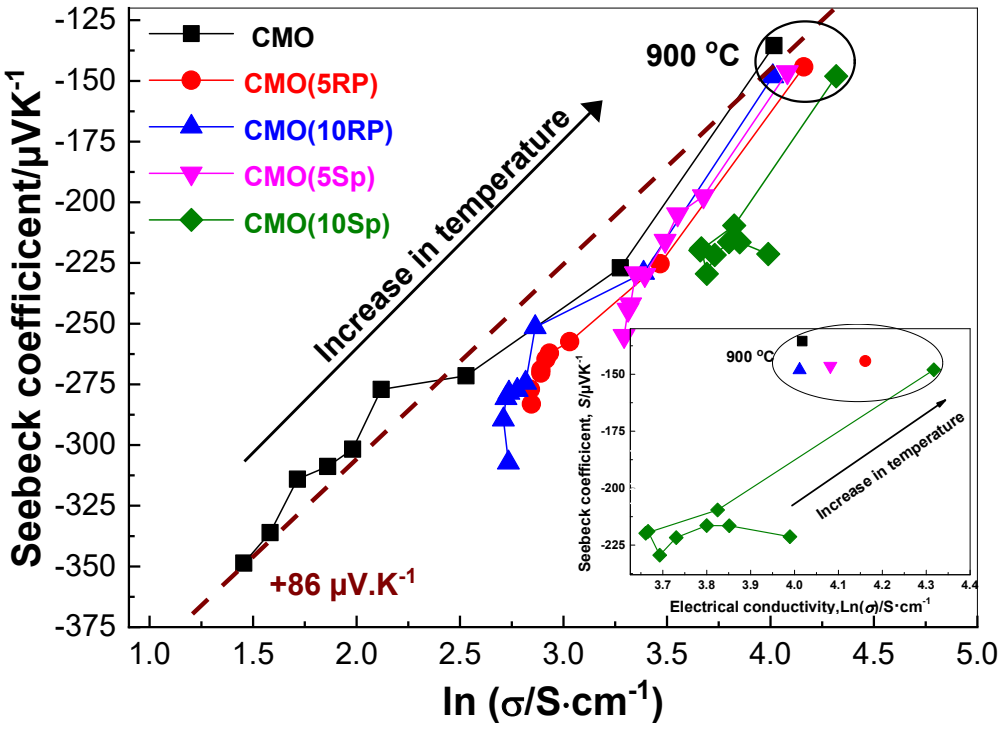

Figure 7. Jonker plot (Eq. 4) based on electrical conductivity and Seebeck coefficients given in Fig. 5a and Fig. 6a. The dashed line corresponds to k/e=+86 μV/K and the remaining lines are guides to the eye. Inset: Magnification of the data for CMO(10Sp).

CMO shows an average slope of +72 μV/K which is in reasonable agreement with the slope predicted in Eq. 3 and supports the assumptions above for pure CMO. All the CMO-composites also show a quite linear behavior at high temperatures although with a somewhat larger slope than predicted by Eq. 3. However, at lower temperatures there are significant deviations. CMO(10SP), in particular, shows large deviations at lower temperatures (inset in Fig. 7) and this may be due to a change in conduction mechanism, shifting from a metallic-like behavior at moderate temperatures to a polaron hopping mechanism at higher temperatures (Fig. 5a). The same explanation may also apply for the other CMO composites although a metallic-like conduction mechanism is not so obvious according to Fig. 5a, and a variable carrier mobility with temperature may also play a role. The degree of orbital degeneracy will also affect the Jonker plot significantly [35], however a more detailed discussion related to degeneracy is beyond the scope of this investigation.

3.3.3. Power factor

The temperature dependences of the power factor, P, are given in Fig. 8. Although the general trend is an increasing $|S|$ from CMO(10Sp) to CMO (Fig. 6a), the power factor is evidently governed by the electrical conductivity (Fig. 5a) showing the highest power factor for the composition with the highest conductivity (CMO(10Sp)) and lowest for CMO. A large power factor is beneficial in applications where electrical power is produced from "infinite heat sources" by thermoelectric generators [4]. From this perspective CMO composites represent a new and cheap material with a noteworthy potential with respect to waste heat harvesting and similar applications, given that the electrical conductivity is enhanced even more by designed structuring at the micro/nano scale. The highest power factor given in Fig. 8 is still somewhat less than values reported for other oxides such as *e.g.* Nd-doped $SrTiO_3$ [3].

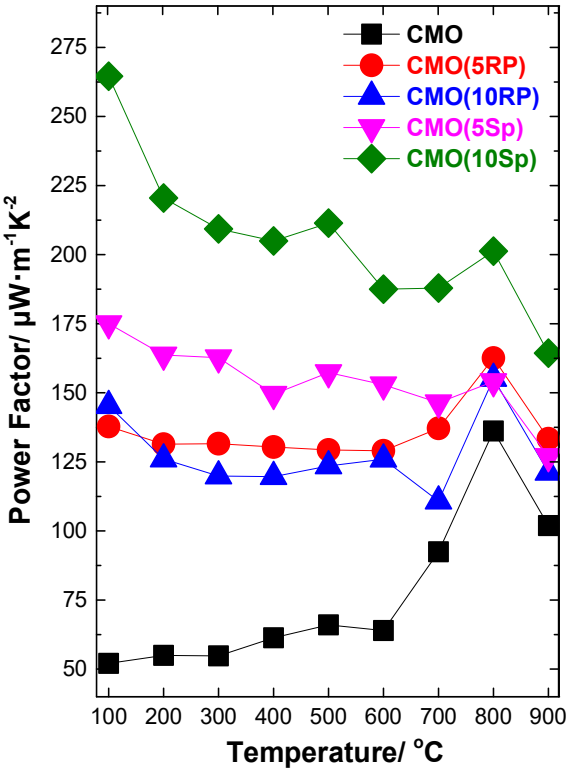

Figure 8. Temperature dependence of the power factor ($P = \sigma \cdot S^2$) for CMO and CMO-composites measured in synthetic air.

3.3.4. Thermal conductivity

The variation in thermal conductivity with temperature for CMO and CMO-composites is given in Fig. 9a. All materials show a declining thermal conductivity with increasing temperature, in accordance with the phonon mean free path being inversely proportional to the absolute temperature. The variation in thermal conductivity between the various materials is small, however the general trend is that at T < 400 °C, CMO(10Sp) exhibits the highest κ, whereas CMO exhibits the lowest. At $T > 400$ °C the stacking order with respect to κ is seen to be reversed and CMO(10Sp) displays the lowest thermal conductivity all the way up to 800 °C. The observed thermal conductivity values for all samples are large as expected for materials with large grains and high densities and are comparable to values reported in the literature for pristine CMO [20]. The thermal conductivity was assessed up to a maximum temperature of 800 °C, which is below the phase transition to a cubic structure.

An enhanced thermal conductivity above the transition temperature is both anticipated and documented in the literature. Thiel *et al.* [20] observed a distinct increase in κ for pristine CMO above 850 °C, coinciding with the phase transition to a cubic structure. The implication of this enhancement will be further commented in the next section.

The variation in κ with temperature for the pure RP and Sp phases is given in Fig. 9b. At $T > 100$ °C the Sp phase shows the highest thermal conductivity at all temperatures. The lower κ for the RP phase is interpreted as a combination of a higher porosity compared with the Sp phase (Tab. 2) and the general crystallographic structure of RP phases with alternating layers of perovskite and rock salt units. The internal interfaces between these units are known to be effective scattering agents for phonons resulting in reduced thermal conductivity [36].

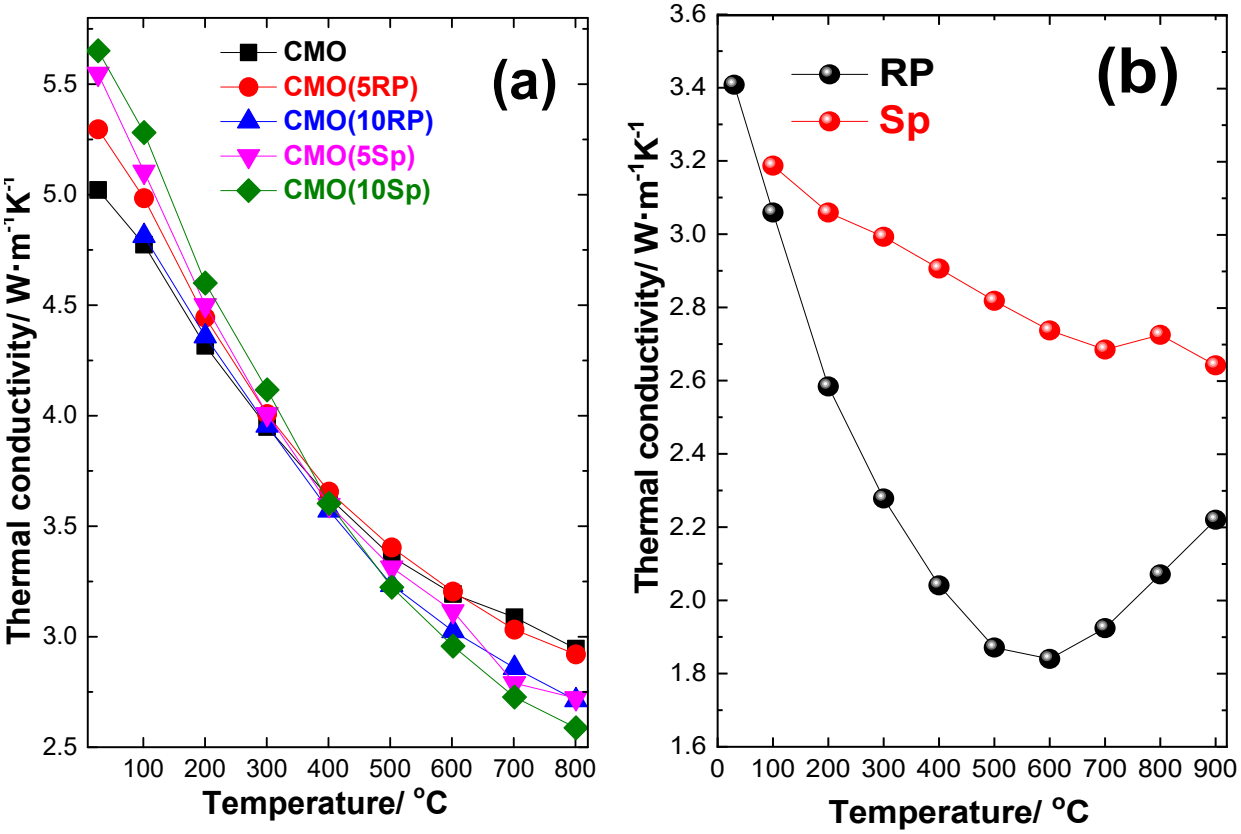

Figure 9. Temperature dependence of thermal conductivity (± 6 %) in synthetic air of (a) CMO and CMO-composites and (b) Ruddlesden-Popper (RP) (black) and spinel (Sp) (red).

3.3.5. Figure-of-merit, zT

The variation in zT with temperature is presented in Fig. 10a and the presence of the secondary phases enhances the zT at all temperatures. The highest zT observed for CMO(10Sp), reaching 0.083 at 800 °C, is governed by the enhanced electrical conductivity (Fig. 5a). In Fig. 10b, we compare our best results with the state-of-the-art data for undoped CMO from the literature. At $T \leq 700$ °C, the zT values reported in [19-22] are all lower than for CMO(10Sp). However, at 800 °C, Thiel *et al.* [20] report values above the CMO composite reaching about 0.12. The main reason for the enhanced zT values reported at 800 °C is due to their reduced thermal conductivity combined with a higher $|S|$. Since our thermal conductivity data is limited up to 800 °C, we are not able to report values for zT at 900 °C. The phase transition to a cubic structure taking place above 900 °C [11] will increase the thermal conductivity and an increase corresponding to a factor of approx. 1.8 has been reported for pristine CMO above 900 °C [20]. Although the increase in κ is somewhat compensated by an enhanced σ (Fig. 5), the corresponding reduction in $|S|$ is significant (Fig. 6a) and a reduction in zT is anticipated at T>800 °C.

We have demonstrated that applying a novel exsolution synthesis route we have prepared CMO-composites with significantly enhanced electrical conductivity and improved zT values compared to pristine $CaMnO_3$. A further refinement of the composite microstructure by combining nanosized precursor powders and alternative sintering methods, such as spark plasma sintering (SPS), may revitalize undoped $CaMnO_3$ as a candidate *n-type* material in all oxide thermoelectric devices for applications at high temperatures in ambient air. It is anticipated that the same approach may further enhance the thermoelectric properties of donor doped CMO. Notably, CMO is attractive also from an environmental point of view as it is based on cheap (abundant) and nontoxic raw materials.

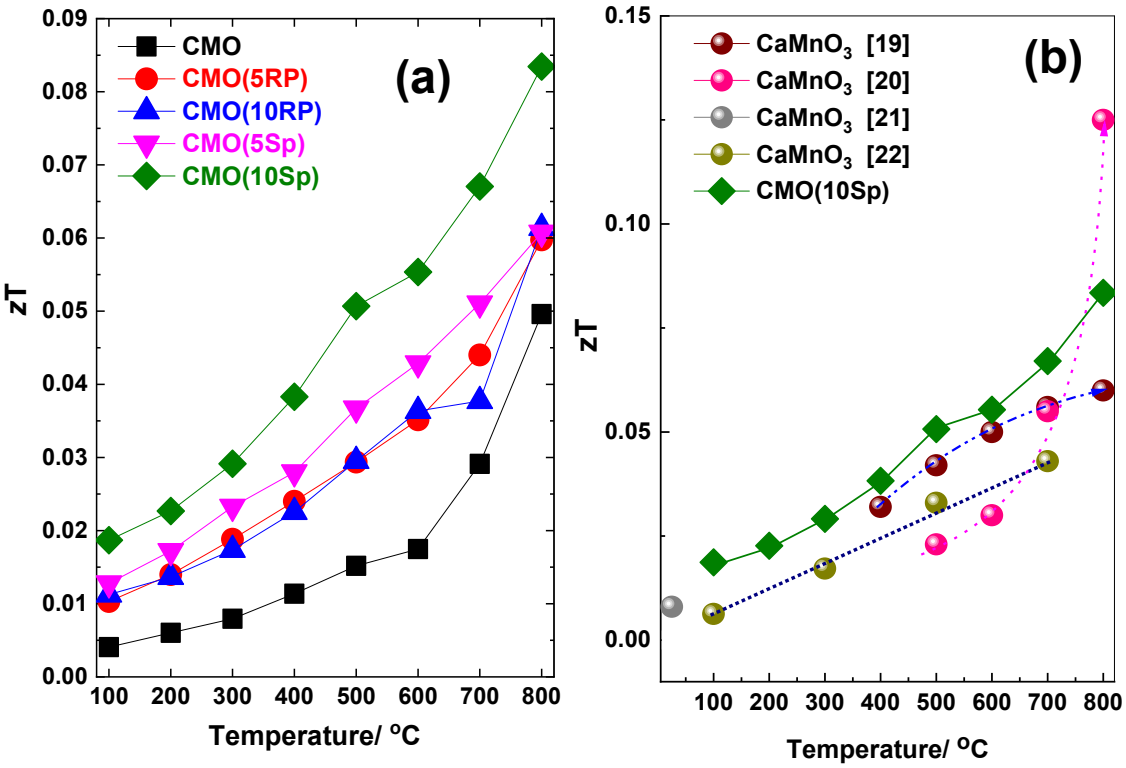

Figure 10. Temperature dependence of the dimensionless figure-of-merit (zT) for a) CMO and CMO composites and b) comparing literature values for pristine CMO [19-22] with CMO(10Sp) from this work.

4. Conclusion

A novel synthesis method for producing well-defined composites of $CaMnO_3$ (CMO) based on exsolution has been developed. Samples corresponding to stoichiometric CMO and CMO-composites with 5 and 10 vol % of RP- and Sp-phases, respectively, were prepared with densities >91 %. The presence of secondary phases significantly enhanced the electrical conductivity compared to pristine CMO. The highest electrical conductivity was observed for CMO composites with 10 vol % Sp, apparently changing conductivity mechanism from a metallic-like at low temperatures to a polaron hopping type at higher temperatures, corresponding 55 S/cm at ambient temperatures and 75 S/cm at 900 °C. This composite also exhibited the highest figure-of-merit (zT) in this study, reaching 0.083 at 800 °C. Although the increase in zT is moderate a further refinement of the composite microstructure with emphasis on increasing the density of interfaces, may

revitalize undoped $CaMnO_3$ as a candidate *n-type* material in all oxide thermoelectric devices for applications at high temperatures in ambient air. It is considered that the new synthesis route developed has the potential to enhance thermoelectric properties also for doped CMO-based composites.

Acknowledgements

Financial support from The Research Council of Norway under the program Nano2021 to the project (number 228854) "Thermoelectric materials: Nanostructuring for improving the energy efficiency of thermoelectric generators and heat- pumps" (THELMA) conducted by NTNU, UiO, SINTEF, IFE, FFI, UiS and UiA is gratefully acknowledged.

References

1. S. LeBlanc, Thermoelectric generators: Linking material properties and systems engineering for waste heat recovery applications. *Sustainable Materials and Technologies*, 2014. **1**(Supplement C): p. 26-35.
2. A. F. Loffe, Semiconductor Thermoelements and Thermoelectric Cooling, English edition. 1957: *Info-search ltd.* London. 184 pages.
3. D. Ekren, F. Azough, A. Gholinia, S. J. Day, D. Hernandez-Maldonado, D. M. Kepaptsoglou, Q. M. Ramasse, R. Freer, Enhancing the thermoelectric power factor of $Sr_{0.9}Nd_{0.1}TiO_3$ through control of the nanostructure and microstructure, *J. Mater. Chem. A,* 2018. 6, 24928-24939
4. M. Bittner, N. Kanas, R. Hinterding, F. Steinbach, J. Räthel, M. Schrade, K. Wiik, M.-A. Einarsrud and A. Feldhoff, A comprehensive study on improved power materials for high-temperature thermoelectric generators, *Journal of Power Sources*, 2019. 410-411, p. 143-151.
5. M. Bittner, N. Kanas, R. Hinterding, F. Steinbach, D. Groeneveld, P. Wemhoff, K. Wiik, M.-A. Einarsrud and A. Feldhoff, Triple-phase ceramic 2D nanocomposite with enhanced thermoelectric properties, *J. Eur. Ceram. Soc.*, 2019. 39, p. 1237-1244.
6. S. G. Jeffrey and E. S. Toberer, Complex thermoelectric materials. *Nat. Mater*, 2008. **7**(2): p. 105-114.
7. M. Shikano, and R. Funahashi, Electrical and thermal properties of single-crystalline $(Ca_2CoO_3)_{0.7}CoO_2$ with a $Ca_3Co_4O_9$ structure. *Appl. Phys. Lett.*, 2003. **82**(12): p. 1851-1853.
8. L. Han, N. V. Nong, W. Zhang, L. T. Hung, T. Holgate, K. Tashiro, M. Ohtaki, N. Pryds, and S. Linderoth, Effects of morphology on the thermoelectric properties of Al-doped ZnO. *RSC Advances*, 2014. **4**(24): p. 12353-12361.

9. L. Han, D. V. Christensen, A. Bhowmik, S. B. Simonsen, L. T. Hung, E. Abdellahi, Y. Z. Chen, N. V. Nong, S. Linderoth and N. Pryds, Scandium-doped zinc cadmium oxide as a new stable n-type oxide thermoelectric material. *J. Mater. Chem. A*, 2016. **4**(31): p. 12221-12231.
10. H. S. Horowitz, and J. M. Longo, Phase Relations in the Ca-Mn-O System. *Mat. Res. Bull.*, 1978. **13**(12): p. 1359-1369.
11. H. Taguchi, M. Nagao, T. Sato, and M. Shimada, High-temperature phase transition of $CaMnO_{3-\delta}$. J. *Solid State Chem.*, 1989. **78**(2): p. 312-315.
12. M. Schrade, R. Kabir, S. Li, T. Norby, and T. G. Finstad, High temperature transport properties of thermoelectric $CaMnO_{3-\delta}$— Indication of strongly interacting small polarons. *J. Appl. Phys*., 2014. **115**(10): p. 103705.
13. E. I. Leonidov, I. A. Leonidov, M. V. Patrakeev, and V. L. Kozhevnikov, Oxygen non-stoichiometry, high-temperature properties, and phase diagram of $CaMnO_{3-\delta}$. *J. Solid State Electrochem.*, 2011. **15**(5): p. 1071-1075.
14. E. Bakken, J. B. Goates, T. Grande, B. Hovde, T. Norby, L. Rørmark, R. Stevens, and S. Stølen, *Entropy of oxidation and redox energetics of $CaMnO_{3-d}$. Solid State Ionics*, 2005. **176**: p. 2261–2267.
15. E. Bakken, T. Norby, and S. Stølen, *Nonstoichiometry and reductive decomposition of $CaMnO_{3-\delta}$. Solid State Ionics*, 2005. **176**(1): p. 217-223.
16. Y. Zhu, C. Wang, W. Su, J. Li, J. Liu, Y. Du and L. Mei, High-temperature thermoelectric performance of $Ca_{0.96}Dy_{0.02}RE_{0.02}MnO_3$ ceramics (RE=Ho, Er, Tm). *Ceram. Int.*, 2014. **40**(10, Part A): p. 15531-15536.
17. W. B. Su, J. Liu, Y. C. Zhou, J. Li, X. Zhang, Y. Du and C. L. Wang, Effects of Dy and Yb co-doping on thermoelectric properties of $CaMnO_3$ ceramics. *Ceram. Int.*, 2015. **41**(1, Part B): p. 1535-1539.
18. L. Bocher, M. H. Aguierre, D. Logvinovich, A. Shkabko, R. Robert, M. Trottman, and A. Weidenkaff, $CaMn_{1-x}Nb_xO_3$ ($x \leq 0.08$) perovskite-type phases as promising new high-temperature n-type thermoelectric materials, *Inorg. Chem.*, 2008. **47**: p. 8077-8085.
19. Y. H. Zhu, W. B. Su, J. Liu, Y. C. Zhou, J. Li, X. Zhang, Y. Du, and C. L. Wang, Effects of Dy and Yb co-doping on thermoelectric properties of $CaMnO_3$ ceramics. *Ceram. Int.*, 2015. **41**(1 part B): p. 1535 - 1539.
20. P. Thiel, J. Eilertsen, S. Populoh, G. Saucke, M. Döbeli, A. Shkabko, L. Sagarna, L. Karvonen, and A. Weidenkaff, Influence of tungsten substitution and oxygen deficiency on the thermoelectric properties of $CaMnO_{3-\delta}$. *J. Appl. Phys.*, 2013. **114**: p. 243707.
21. A. Bhaskar, J. J. Yuan, and C. J. Liu, Thermoelectric properties of n-type $Ca_{1-x}Bi_xMnO_{3-\delta}$ (0.00, 0.02, and 0.05) system. *J. Electroceram.*, 2013. **31**(1): p. 124 - 128.
22. D. Flahaut, R. Funahashi, K. Lee, H. Ohta, and K. Koumoto, Effect of the Yb substitutions on the thermoelectric properties of $CaMnO_3$, *25th International Conference on Thermoelectrics*. 2006, IEEE: Vienna. p. 103 - 106.
23. T. E. Loland, J. Sele, M.-A. Einarsrud, P. E. Vullum, M. Johnsson, and K.Wiik, *Thermal Conductivity of A-Site Cation-Deficient La-Substituted $SrTiO_3$ Produced by Spark Plasma Sintering.* Energy Harvesting and Systems, 2015. **2**(1-2): p. 63-71.
24. F. P. Glasser, The ternary system CaO-MnO-SiO_2, *J. Am. Ceram. Soc.*, 1962. **45**: p. 242-249.
25. A. Muan and E. F. Osborn, Phase equilibria among oxides in steelmaking, *Addison Wesley Publishing Company, Inc.*, 1965.

26. L. Rioja-Monllor, C. Bernuy-Lopez, M.-L. Fontaine, T. Grande and M.-A. Einarsrud. Processing of high performing composite cathodes for protonic ceramic fuel cells by exsolution, *J. Mater. Chem.*, 2019. A7: p. 8609-8619.
27. K. Nakade, K. Hirota, M. Kato, and H. Taguchi, Effect of the Mn^{3+} ion on electrical and magnetic properties of orthorhombic perovskite-type $Ca(Mn_{1-x}Ti_x)O_{3-\delta}$. *Mater. Res. Bull.*, 2007. **42**(6): p. 1069-1076.
28. K. R. Poeppelmeier, H. S. Horowitz, and J. M. Longo, Oxide solid solutions derived from homogeneous carbonate precursors: The CaO-MnO solid solution. *Journal of the Less Common Metals*, 1986. **116**(1): p. 219-227.
29. C. Brisi, and M.L. Borlera, A new compound in the system $CaO{\cdot}MnO_2$. *J. Inorg and Nucl. Chem.*, 1965. **27**(9): p. 2129-2132.
30. S. Zouari, L. Ranno, A. C. Rouhou, O. Isnard, M. Pernet, P. Wolfers, and P. Strobel, New model for the magnetic structure of the marokite-type oxide $CaMn_2O_4$. *J. Alloys Compd*, 2003. **353**(1): p. 5-11.
31. I. Wærnhus, T. Grande, and K. Wiik, Surface exchange of oxygen in $La_{1-x}Sr_xFeO_{3-\delta}$ (x=0, 0.1), *Top. Catal.*, 2011. **54**: p. 1009-1015.
32. N. Pryds, and V. Esposito, When two become one: An insight into 2D conductive oxide interfaces, *J. Electroceram,* 2017. **38**: p. 1-23.
33. S. Thiel, G. Hammerl, A. Schmehl, C.W. Schneider, and J. Mannhart, Tunable Quasi-Two-Dimensional Electron Gases in Oxide Heterostructures. *Science*, 2006. **313**(5795): p. 1942.
34. G. H. Jonker, The application of combined conductivity and seebeck- effect plots for the analysis of semiconductor properties. *Philips Res. Repts* 1968. **23**: p. 131 - 138.
35. Z. Qimin, H. E. Mitchell, J. I. Brian, and O. M. Thomas, Combined Jonker and Ioffe Analysis of Oxide Conductors and Semiconductors. *J. Am. Ceram. Soc.*, 2011. **94**(1): p. 187-193.
36. K. H. Lee, S. W. Kim, H. Ohta, and K. Koumoto, Ruddlesden-Popper phases as thermoelectric oxides: Nb-doped $SrO(SrTiO_3)n$ (n=1,2). *J. Appl. Phys.*, 2006. **100**(6): p. 063717.